Title
Fast-ion transport induced by Alfvén eigenmodes in the ASDEX Upgrade tokamak

Journal
Nuclear Fusion, 51(10)

ISSN
0029-5515

Authors
Garcia-Munoz, M
Classen, IGJ
Geiger, B
et al.

Publication Date
2011

DOI
10.1088/0029-5515/51/10/103013

IOP Publishing and International Atomic Energy Agency Nuclear Fusion

Nucl. Fusion **51** (2011) 103013 (14pp) doi:10.1088/0029-5515/51/10/103013

Fast-ion transport induced by Alfvén eigenmodes in the ASDEX Upgrade tokamak

M. Garcia-Munoz[1], I.G.J. Classen[2], B. Geiger[1], W.W. Heidbrink[3], M.A. Van Zeeland[4], S. Äkäslompolo[5], R. Bilato[1], V. Bobkov[1], M. Brambilla[1], G.D. Conway[1], S. da Graça[6], V. Igochine[1], Ph. Lauber[1], N. Luhmann[7], M. Maraschek[1], F. Meo[8], H. Park[9], M. Schneller[1], G. Tardini[1] and the ASDEX Upgrade Team

[1] Max-Planck-Institut für Plasmaphysik, EURATOM Association, Garching, Germany
[2] FOM-Institute for Plasma Physics Rijnhuizen, EURATOM Association, The Netherlands
[3] University of California-Irvine, Irvine, CA 92697, USA
[4] General Atomics, San Diego, CA 92186-5608, USA
[5] Helsinki University of Technology, Association EURATOM-TEKES, Finland
[6] Associacao EURATOM/IST, Instituto de Plasmas e Fosao Nuclear – Laboratorio Associado, IST, Lisbon, Portugal
[7] University of California at Davis, Davis, CA 95616, USA
[8] Association Euratom-Risø National Laboratory for Sustainable Energy, Technical University of Denmark, DK-4000 Roskilde, Denmark
[9] POSTECH, Pohang, Gyeongbuk, 790-784, Korea

E-mail: Manuel.Garcia-Munoz@ipp.mpg.de

Received 2 February 2011, accepted for publication 21 July 2011
Published 19 August 2011
Online at stacks.iop.org/NF/51/103013

Abstract

A comprehensive suite of diagnostics has allowed detailed measurements of the Alfvén eigenmode (AE) spatial structure and subsequent fast-ion transport in the ASDEX Upgrade (AUG) tokamak [1]. Reversed shear Alfvén eigenmodes (RSAEs) and toroidal induced Alfvén eigenmodes (TAEs) have been driven unstable by fast ions from ICRH as well as NBI origin. In ICRF heated plasmas, diffusive and convective fast-ion losses induced by AEs have been characterized in fast-ion phase space. While single RSAEs and TAEs eject resonant fast ions in a convective process directly proportional to the fluctuation amplitude, $\delta B/B$, the overlapping of multiple RSAE and TAE spatial structures and wave–particle resonances leads to a large diffusive loss, scaling as $(\delta B/B)^2$. In beam heated discharges, coherent fast-ion losses have been observed primarily due to TAEs. Core localized, low amplitude NBI driven RSAEs have not been observed to cause significant coherent fast-ion losses. The temporal evolution of the confined fast-ion profile in the presence of RSAEs and TAEs has been monitored with high spatial and temporal resolution. A large drop in the central fast-ion density due to many RSAEs has been observed as $q_{\rm min}$ passes through an integer. The AE radial and poloidal structures have been obtained with unprecedented details using a fast SXR as well as 1D and 2D ECE radiometers. GOURDON and HAGIS simulations have been performed to identify the orbit topology of the escaping ions and study the transport mechanisms. Both passing and trapped ions are strongly redistributed by AEs.

(Some figures in this article are in colour only in the electronic version)

1. Introduction

Future burning plasma experiments such as ITER may be subject to the excitation of Alfvén eigenmode (AE) instabilities [2] by 3.5 MeV fusion born alpha particles as well as fast ions created by auxiliary heating systems [3, 4]. If allowed to grow unabated, these instabilities have the potential to cause fast-ion redistribution and loss leading to a degradation of the fusion performance, heating and current drive efficiencies [5, 6] as well as to possible serious damage of first wall components [7]. Of special importance to magnetically confined fusion plasmas are toroidal Alfvén eigenmodes (TAEs) [8, 9] and reverse shear Alfvén eigenmodes (RSAEs) [10–15] because of their potential to eject fast ions before their thermalization [6, 16]. On the road to address these issues, significant progress in fast-ion physics has been made recently on ASDEX Upgrade

(AUG). An extended suite of diagnostics now allows detailed measurements of AE spatial structure and the subsequent fast-ion transport. Fast 1D and 2D imaging [17] electron cyclotron emission (ECE) measurements of the temperature fluctuations induced by the AEs have delivered unprecedented details on eigenmode radial and poloidal structure. Apart from the recently installed ECE-imaging (ECEI) system, the upgraded fluctuation diagnostics, used in these studies, include 1D ECE [18], soft x-ray (SXR) [19] and reflectometry [20]. The main systems utilized to diagnose the fast-ion internal redistribution and eventual loss are the neutron rates [21], the fast-ion D-alpha (FIDA) spectroscopy [22] and the scintillator based fast-ion loss detectors (FILDs) [23]. An overview of the AUG diagnostics utilized in this work is shown in figure 1. FIDA spectroscopy has recently been developed at AUG [24] following the technique employed for the first time at DIII-D [22] and more recently at TEXTOR [25], NSTX [26] and LHD [27]. The upgraded AUG FILDs provide energy and pitch-angle resolved measurements of fast-ion losses with a bandwidth of 1 MHz at two different toroidal positions and ≈30 cm above the midplane. The AUG FILD design is based on the concept of the α-particle detector used for the first time on the TFTR tokamak [28, 29] and more recently on several fusion devices such as CHS [30], W7-AS [31, 32], LHD [33], JET [34], NSTX [35], TJ-II [36] and DIII-D [37, 38].

Over the past two years, experiments have been conducted in AUG to study the fast-ion transport due to AEs in plasmas heated purely by ICRH or NBI. In ICRH heated plasmas, strong fast-ion losses induced by RSAEs and TAEs have been observed correlated with a neutron rate drop of ≈50% [39, 40]. Time-resolved energy and pitch-angle measurements of fast-ion losses correlated in frequency and phase with RSAEs and TAEs have allowed clear identification of the loss mechanisms. In NBI heated plasmas, RSAEs and TAEs have been driven unstable during the current ramp-up phase when incomplete current penetration results in a high central safety factor and strong drive due to multiple higher order resonances [41]. Core localized, low amplitude NBI driven RSAEs have not been observed to cause significant coherent fast-ion losses. The fast-ion redistribution due to RSAEs and TAEs has been measured using the recently developed in AUG FIDA spectroscopy.

This paper is divided into two sections devoted to the study of the AE induced fast-ion transport in ICRH (section 2) and NBI (section 3) heated discharges. In section 2.1, an overview of the main plasma parameters is presented together with the observed AE activity in ICRH heated discharges. The nature and radial structures of the AEs are analysed by means of the AUG magnetic pick-up coils, SXR and 1D ECE diagnostics together with simulations performed with the NOVA code. Section 2.2 is dedicated to the fast-ion losses observed in the presence of these AEs. Time-resolved fast-ion loss measurements show a linear and quadratic dependence on the AE fluctuation amplitude which indicate the convective and diffusive character of the loss mechanisms. Preliminary modelling results are presented to identify the topology of the measured escaping ions and the possible wave–particle resonances that may be causing the fast-ion losses. Section 3.1 is dedicated to the AE activity measured with the AUG 2D ECE imaging and reflectometer systems in NBI heated discharges. The neutron rate during the first phase of the discharges is shown to give the reader an idea of the global impact that AEs have on the fast-ion confinement. In section 3.2, the AE induced fast-ion redistribution and loss measured by the FIDA system and FILD detectors, respectively, are presented. The weighting function of the new FIDA diagnostic at AUG is also briefly introduced in order to make a direct comparison between FIDA and FILD measurements.

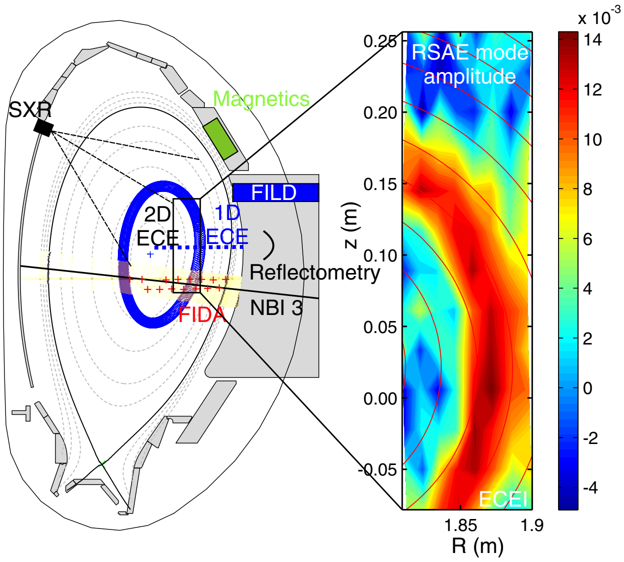

Figure 1. AUG poloidal cross section showing an overview of the relevant diagnostics for AE studies. On the right, the typical radial structure of a RSAE measured by the 2D ECE-imaging system is shown.

2. Alfvén eigenmodes and associated fast-ion transport in ICRF heated discharges

An important difference between present experiments and ITER will be the presence of fusion born α-particles as main heating source. These MeV α-particles with relatively small characteristic orbit lengths (compared with plasma minor radius), velocities well above the Alfvén velocity, and an isotropic distribution function will likely excite meso-scale fluctuations. In contrast, in present experiments, fast ions are mainly generated by external heating systems with highly anisotropic distribution functions that typically excite macro-scale collective modes (e.g. AEs). While RF heating systems mostly populate the fast-ion phase space corresponding to deeply trapped supra-Alfvénic ions, NBI systems, depending on their injection geometries, mainly create a large population of supra-thermal (in some cases even supra-Alfvénic) passing ions. In general, minority and high-harmonic RF heating constitute a unique tool to achieve some burning-relevant dynamical regimes with ions in the MeV range.

2.1. Alfvén eigenmodes

In AUG, on-axis minority RF heating in low density deuterium plasmas create a large population of supra-Alfvénic ions that usually drive a rich variety of Alfvén/Alfvén-acoustic eigenmodes [42]. The experiments discussed here have been performed in plasmas with plasma current $I_p \approx 0.8$ MA,

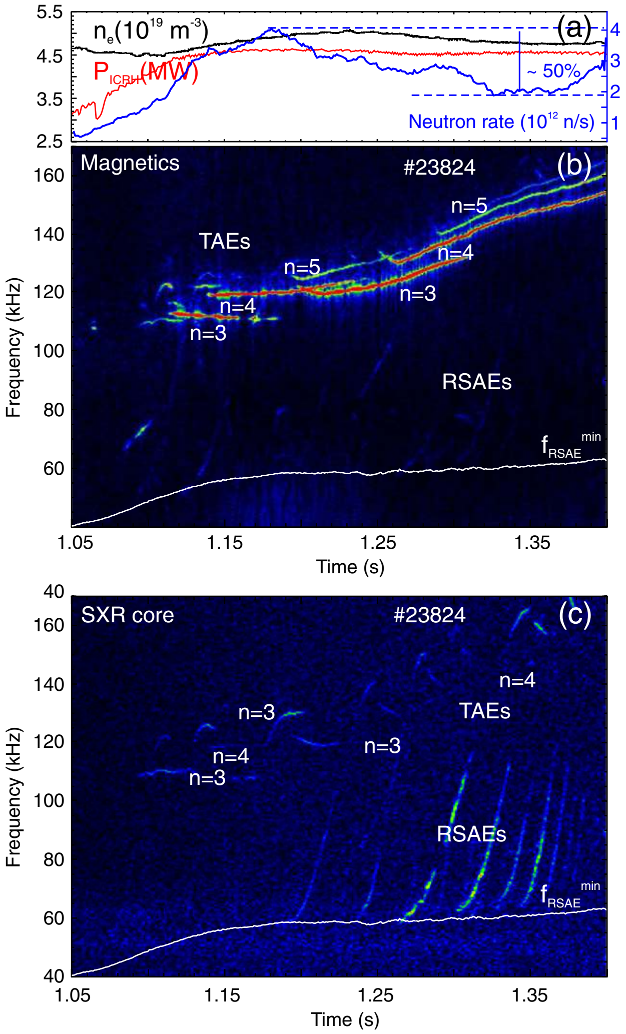

Figure 2. AUG discharge #23824. (*a*) Core line integrated electron density, n_e, neutron rate and ICRH power (dashed line), P_{ICRH}. (*b*) Spectrogram of an in-vessel magnetic pick-up coil. (*c*) Spectrogram of a core SXR channel.

toroidal field $B_t = 2.0\,\mathrm{T}$, safety factor at the edge $q_{95} \approx 4.0$ and ion cyclotron resonance heating (ICRH) as main heating and fast-particle source. 4.5 MW of on-axis ICRF hydrogen minority heating was applied to a deuterium plasma ($n_H/n_D \approx 5\%$). In figure 2(*a*), the core line integrated electron density, n_e, applied ICRH power and neutron rate of the baseline discharge, #23824, are presented. Figures 2(*b*) and (*c*) show, respectively, the Fourier spectrograms for a magnetic fluctuation signal and for a SXR signal corresponding to a line of sight passing through the plasma core. Several coherent MHD fluctuations are visible around 110 kHz up to 170 kHz. They correspond to TAEs with different toroidal mode numbers, $n = 3, 4, 5$, as obtained from Mirnov coils, whose presence is confirmed also by comparison with ideal MHD calculations carried out with the NOVA code [43]. Magnetic fluctuations chirping in frequency from ≈50 kHz up to the TAE frequencies (barely visible in the magnetics spectrogram) have been identified as RSAEs by means of the SXR emission from the plasma core as figure 2(*c*) shows. The lowest RSAE frequency, $f_{\mathrm{RSAE}}^{\mathrm{min}}$, in figure 2(*b*) and (*c*) is mainly given by the geodesic compressibility and the toroidal coupling to the acoustic waves, as expected by the theory [44]. Pressure effects modify the local dispersion relation for shear Alfvén waves in low-β plasmas: $\omega_{\mathrm{RSAE}} \approx |\frac{m}{q_{\mathrm{min}}-n}| \cdot \frac{V_A}{R_0}$, with m the poloidal mode number. The modified minimum of the local dispersion relation is then given by the geodesic acoustic frequency:

$$\omega_{\mathrm{geo}}^{\mathrm{min}} \approx \frac{\sqrt{2}}{R_0} \cdot C_s = \frac{\sqrt{2}}{R_0} \cdot \left(\frac{T_i}{m_i}\right)^{1/2} \cdot \left(\frac{7}{4} + \frac{T_e}{T_i}\right)^{1/2}. \qquad (1)$$

An excellent agreement between the experimental lowest RSAE frequency ($f_{\mathrm{RSAE}}^{\mathrm{min}}$) and the modified dispersion relation is clearly visible in figures 2(*b*) and (*c*) (superimposed in white). The estimated $f_{\mathrm{RSAE}}^{\mathrm{min}}$ has been calculated assuming $T_e = T_i$ and taking T_e from an ECE channel near the RSAE localization and assuming a negligible plasma rotation.

Fluctuations in the electron temperature profile caused by the RSAEs and TAEs [45] have been measured with the 1D ECE radiometer. The RSAE and TAE radial structures have been reconstructed by means of ECE-FILD cross-correlation techniques to improve signal-to-noise ratios. Figures 3(*a*)–(*c*) show the normalized crosspower spectral densities (coherence) as a function of ρ_{pol} and frequency for 50 ms time intervals. The RSAE and TAE radial structures were obtained by selecting and averaging a certain frequency band of the coherence. The selected RSAE and TAE frequency bands are given in figures 3(*a*)–(*c*). Figure 3(*a*) shows global TAEs extended from $\rho_{\mathrm{pol}} \approx 0.23$ up to the edge with broad RSAEs localized at $\rho_{\mathrm{pol}} \approx 0.4$. A complete overlapping of RSAE–TAE radial structures is clearly visible (highlighted in yellow). Figure 3(*b*) shows the RSAE–TAE radial structures for a later time interval. TAEs shift outwards becoming more localized while RSAEs shift inwards becoming also more localized at $\rho_{\mathrm{pol}} \approx 0.3$. The overlapping region becomes smaller. Finally, figure 3(*c*) shows a negligible RSAE–TAE spatial overlapping with RSAEs and TAEs well localized at $\rho_{\mathrm{pol}} \approx 0.3$ and $\rho_{\mathrm{pol}} \approx 0.6$, respectively. The largest RSAEs and TAEs presented here caused a normalized T_e perturbation of $\delta T_e/T_e \approx 0.009$. NOVA simulations have been performed to identify the AEs as well as their spatial structures and radial shifts. In figures 3(*d*)–(*f*) the displacements predicted by NOVA for three different AEs are presented. NOVA calculations used experimental profiles of electron density and electron temperature combined with the assumption of $T_e = T_i$ to obtain the equilibrium pressure information. The q-profile for the NOVA simulations has been inferred from the MHD activity evolution during the plasma discharge, i.e. RSAE, TAE and later sawtooth spatial location and occurrence. Figures 3(*d*)–(*f*) show the radial structures of $n = 3$ RSAE at $q_{\mathrm{min}} = 1.58$, and both $n = 3$ TAEs at $q_{\mathrm{min}} = 1.46$. The different curves in figures 3(*d*)–(*f*) represent the different poloidal harmonics. The timing corresponding to this q_{min} evolution can be identified in figure 4.

A Fourier analysis of the total losses measured by FILD in the presence of the AEs reveals details of the RSAEs, TAEs and RSAE–TAE-transition that are not visible either on the magnetic or on the SXR spectrogram (figures 2(*b*) and (*c*)). The FILD spectrogram of figure 4(*a*) shows the frequency evolution of the RSAEs from the geodesic acoustic frequency up to the TAE frequency with a clear frequency gap at the RSAE–TAE transition between the RSAE and its associated TAE. This apparent frequency-gap has been

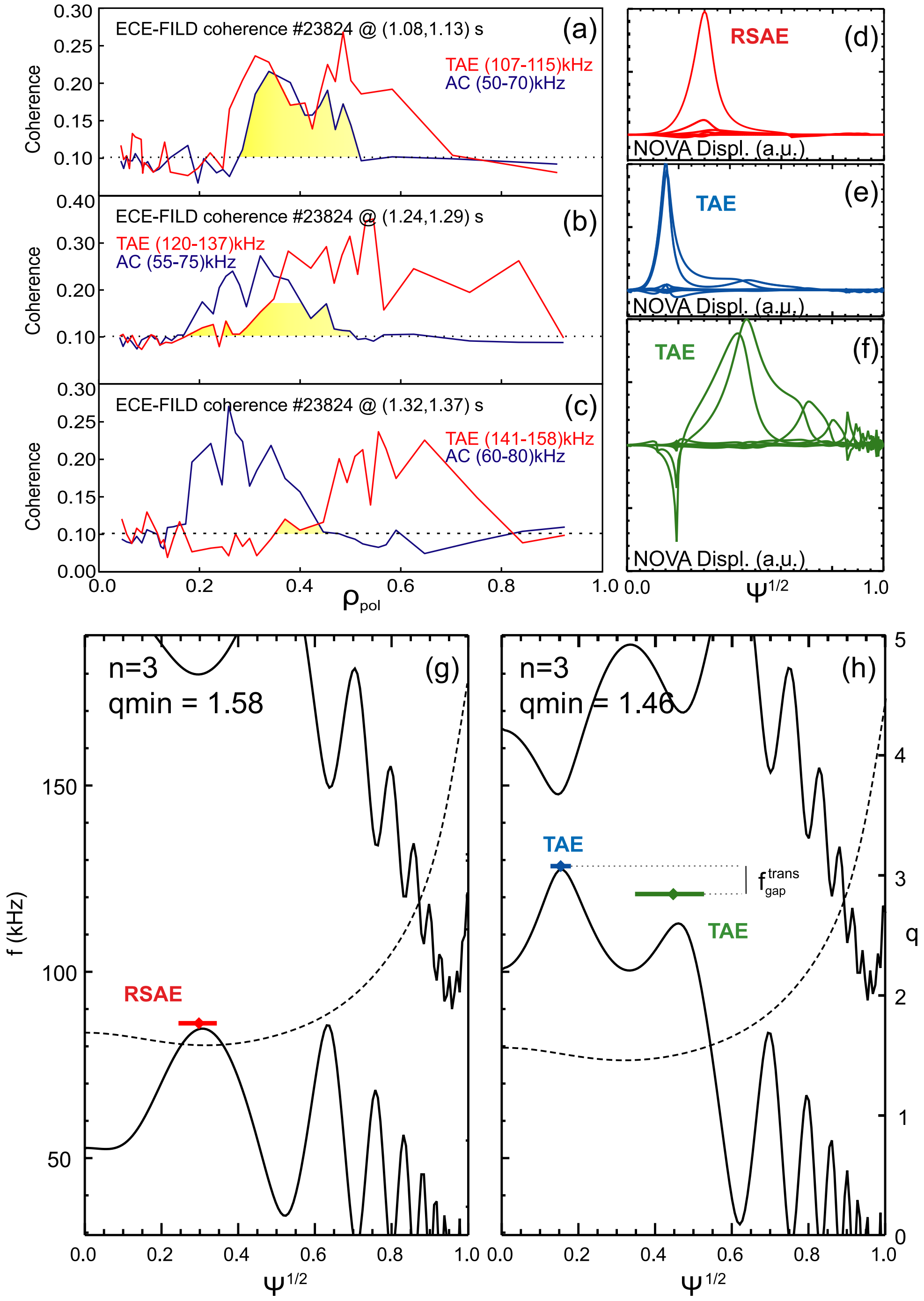

Figure 3. AUG discharge #23824. RSAEs and TAEs radial structures obtained by means of ECE-FILD cross-correlation. The fast-ion losses used for the cross-correlation technique have energies (E) and pitch angles (Λ) $\approx$ (600 keV, 70°). RSAE radial structures are reconstructed at the RSAE lowest frequency. Different time intervals are displayed; (a) for (1.08–1.13) s, (b) for (1.24–1.29) s and (c) for (1.32, 1.37) s. In yellow are highlighted the regions with overlapping TAE–RSAE internal structures well before the RSAE–TAE transition. (d)–(f) $n = 3$ RSAEs and TAE spatial profiles calculated with the NOVA code. (g) and (h) show the Alfvén spectra for the RSAEs and TAEs $n = 3$ at two different time points. The corresponding q-profiles are plotted in dashed lines.

studied using the ideal MHD eigenvalue solver NOVA. The minimum q was successively reduced and the eigenfrequency of modes identified as RSAEs as well as the TAEs resulting from the typical RSAE to TAE transition were recorded for $n = 3$–6. An effect not typically described in the literature, but important here to explain the frequency gap during the RSAE–TAE transition visible on the FILD spectrogram (inset in figure 4(a)), is that it is possible as $q_{\min}$ changes from m/n to $(m - 1/2)/n$, for the RSAE to transition to two separate TAEs each one centred near the $q \approx (m - 1/2)/n$ surface (one on either side of $q_{\min}$) and being composed of the m and $m - 1$ poloidal harmonics. The inset in figure 4(b) shows a zoom of this eigenmode splitting at the transition for the RSAE $n = 5$. The yellow points predicted by NOVA are stable in the plasma

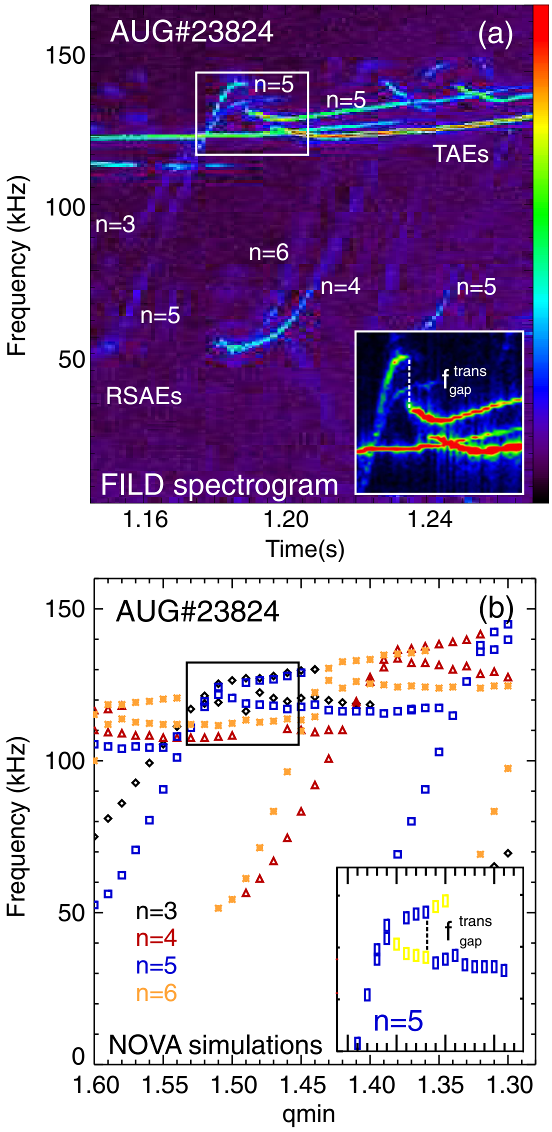

Figure 4. AUG discharge #23824. (*a*) Fourier analysis of the total fast-ion losses with energies (E) and pitch angles (Λ), $(E, \Lambda) \approx (600\,\text{keV}, 70^\circ)$, during the time window (1.14,126) s. The inset shows a zoom of the RSAE–TAE transition frequency gap. (*b*) NOVA simulations of AE activity during the same time window (1.14,126) s. The inset shows the RSAE splitting into two TAEs with different frequencies at transition.

and therefore not visible in the FILD spectrogram. Whether these modes are eigenmodes of the plasma itself is determined by the actual equilibrium pressure gradients, magnetic shear, etc and that observed experimentally is, in a perturbative sense, due to the details of the fast-ion population that provides drive for the eigenmodes. The NOVA calculations reproduce well both the experimentally measured frequency sweeping as well as the actual magnitudes. Note, the effective gamma used in these simulations was $\gamma = (T_e + 7/4T_i)/(T_e + T_i) = 1.375$, which affects the minimum RSAE frequency obtained. The frequency splitting due to the appearance of two separate TAEs (relatively constant frequency modes) from each RSAE frequency sweep also looks similar to that measured experimentally with the difference being that experimentally, only one of the two TAEs from each RSAE transition is observed. Experimentally, the RSAE appears to *jump* to the lower frequency TAE near $q_{\min} \approx (m - 1/2)/n$, which corresponds to the mode at larger minor radius, creating the frequency gap visible on the FILD spectrogram. As mentioned, this is probably due to the details of the fast-ion profile driving the modes and a change in stability from one mode to the other. This stability analysis using a realistic ICRH fast-ion distribution function and a MSE constrained q-profile will be the subject of a future study. However, although the mode stability as well as radial extension depend strongly on the details of the q-profile, the frequency gap observed experimentally during the RSAE–TAE transition, and explained using NOVA simulations follow the basics of the RSAE–TAE general theory for a reversed shear magnetic configuration.

2.2. *Fast-ion transport*

A minimum RF power of ≈3 MW for on-axis minority heating is typically necessary in AUG to drive AEs unstable with energetic ions [46, 47]. In the presence of ICRH driven RSAEs and TAEs strong fast-ion losses are detected by the FILD system [23] correlated with a neutron rate drop of ≈50%, see figure 2(*a*). According to ICRH simulations performed with the TORIC full-wave code [48], about 10% of the ICRH power is absorbed in this discharge directly by deuterium ions at the second harmonic ($\omega = 2\Omega_{cD} = \Omega_{cH}$). The deuterium distribution function presents a clear fast-ion tail, which is responsible for a substantial increase in the neutron rate. Indeed, the neutron rate synthetic diagnostic built in SSFPQL [49] estimates a neutron rate four times higher due to the ICRH than due to the deuterium background alone. This may explain the neutron rate drop as a redistribution of the energetic deuterium ions created by ICRH second-harmonic heating.

In order to fully characterize the orbits of the lost ions and identify the wave–particle resonances responsible for the losses, the phase space (energy and pitch angle at the FILD position) of the fast-ion losses is shown in figure 5. The energy of the lost ions is given by their gyroradius (ρ) and the pitch angle by angle between the ion velocity and the local magnetic field ($\Lambda = \arccos(v_\parallel/v)$). In the presence of multiple AEs, i.e. $t = 1.36$ s, fast ions are ejected within a broad energy range with gyroradius from ≈35 mm up to ≈105 mm, see figure 5(*a*). For the magnetic field at the probe, ≈1.6 T, this gyroradii range corresponds to hydrogen ions with energies between ≈0.2 MeV and ≈1.4 MeV (note that at very large gyroradius (⩾80 mm) the FILD collimator efficiency is rather limited making virtually impossible the identification of different energies). As expected from ICRF heated plasmas the fast-ion losses appear at high pitch angles between 67° and 80°. The velocity space of lost fast ions changes strongly during the evolution of the AE activity, showing a completely different pattern within the next 200 ms. Figure 5(*b*) presents fast-ion losses well localized at high pitch angles (≈71°) and energies (gyroradius ≈60 mm).

The topology of the escaping ions detected by the FILD system has been investigated using the full orbit code GOURDON. The trajectory of the escaping ions has been calculated backwards in time from the detector to the plasma.

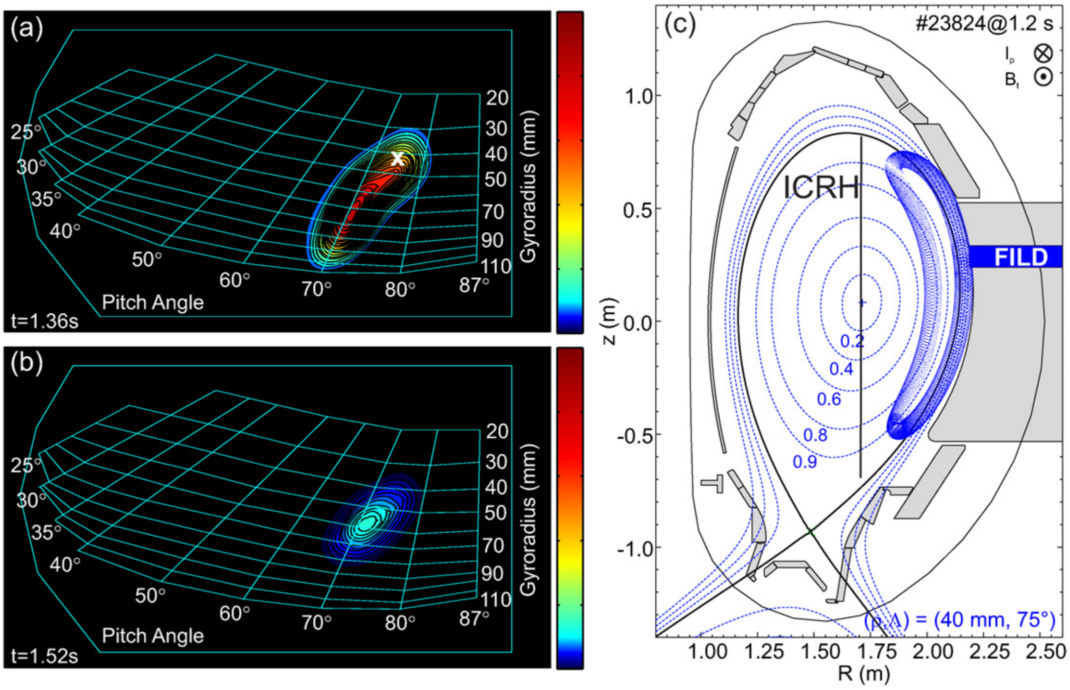

Figure 5. AUG discharge #23824. Phase space of escaping ions. (*a*) Velocity space of escaping ions in the presence of (*a*) many AEs and (*b*) a single $n = 5$ AE. (*c*) Typical trajectory of a lost hydrogen ion with $E = 200$ keV calculated backward in time from detector collimator position to plasma. The vertical black line indicates the position of the ICRH resonance layer.

The particles have been started at the FILD collimator position with the right gyro-phase and the detected energy and pitch angle and followed until they close a full poloidal transit in the absence of AE wave fields. Figure 5(*c*) shows a typical trajectory of an escaping ion.

A Fourier analysis of the fast-ion loss signal allows us to identify the MHD fluctuations responsible for the losses during the entire time window with AE activity, figure 6(*a*). A clear correlation between the TAE frequency pattern and the fast-ion loss frequencies is observed in both magnetics, figure 2(*b*), and FILD, figure 6(*a*), spectrograms during the whole time window. Although all TAEs eject resonant ions, the relative amplitude of the measured losses with respect to the fluctuation amplitude does not depend only on the magnetic fluctuation amplitude e.g. the losses measured at the $n = 4$ TAE frequency are not as strong as one could expect from its large fluctuation amplitude in figure 2(*b*). Changes in the spatial distribution of the losses could explain this observation as the measurements are performed at a single poloidal position. In addition, fast-ion losses chirping in frequency from approximately the geodesic frequency, $f_{\rm RSAE}^{\rm min}$, up to the TAE frequency, $f_{\rm TAE}$, emerge following the typical RSAE frequency pattern. The RSAE induced resonant losses appear stronger (≈10% of the total resonant losses) in the frequency range where the RSAEs interact with the Alfvén-acoustic branch near the $f_{\rm RSAE}^{\rm min}$ and during the RSAE–TAE transition.

The raw data of the Fourier-analysed fast-ion loss signal shown in figure 6(*a*) is presented in figure 6(*b*) to investigate the diffusive and convective character of the losses. The signal consists of a modulated (coherent) signal sitting on an incoherent background (see the inset in figure 6(*b*)) whose amplitude varies with time. The coherent component of the fast-ion losses is correlated in frequency and phase with the corresponding magnetic fluctuation, giving rise to the spectrogram shown in figure 6(*a*). The incoherent component is dominant, up to 80% of the total losses, in the presence of multiple frequency chirping AEs, $t \approx (1.1\text{–}1.3)$ s, and decreases when the number of modes decreases. However, it should be noted that it is not zero when only one mode is ejecting ions with a relatively large amplitude, $t \approx (1.42\text{–}1.52)$ s, as discussed later. During the time window $t \approx (1.52\text{–}1.65)$ s only coherent losses induced by a single TAE, $n = 5$, are visible. Going backwards in time, the incoherent losses of ions with gyroradius ≈60–70 mm appear, for $t \leqslant 1.52$ s, when the local maximum radial displacement of the magnetic field lines is larger than ≈2 mm as measured by its fluctuation induced on the SXR emission. This threshold in the fluctuation amplitude is depicted in figure 6(*b*) with a vertical dashed line.

The basic properties of the coherent and incoherent losses are investigated through their dependence on the magnetic fluctuation amplitude. Tracking the frequencies of the individual fluctuations in both, magnetics and FILD spectrograms, we get the relationship between the coherent fast-ion losses and the corresponding magnetic fluctuation amplitude. Figure 6(*c*) shows this exercise for the TAE $n = 3$ between $t = 1.24$ s and $t = 1.32$ s. A clear linear dependence is visible during the whole time window, showing the convective character of the underlying loss mechanism. A similar analysis has been done for the incoherent losses shown in figure 6(*d*). The envelope of the incoherent losses, black curve in figure 6(*b*), is plotted in figure 6(*d*) as a function of the amplitude of the TAE $n = 5$ for a time interval close to the onset of the incoherent losses, inset in figure 6(*d*), $t = (1.42, 1.50)$ s.

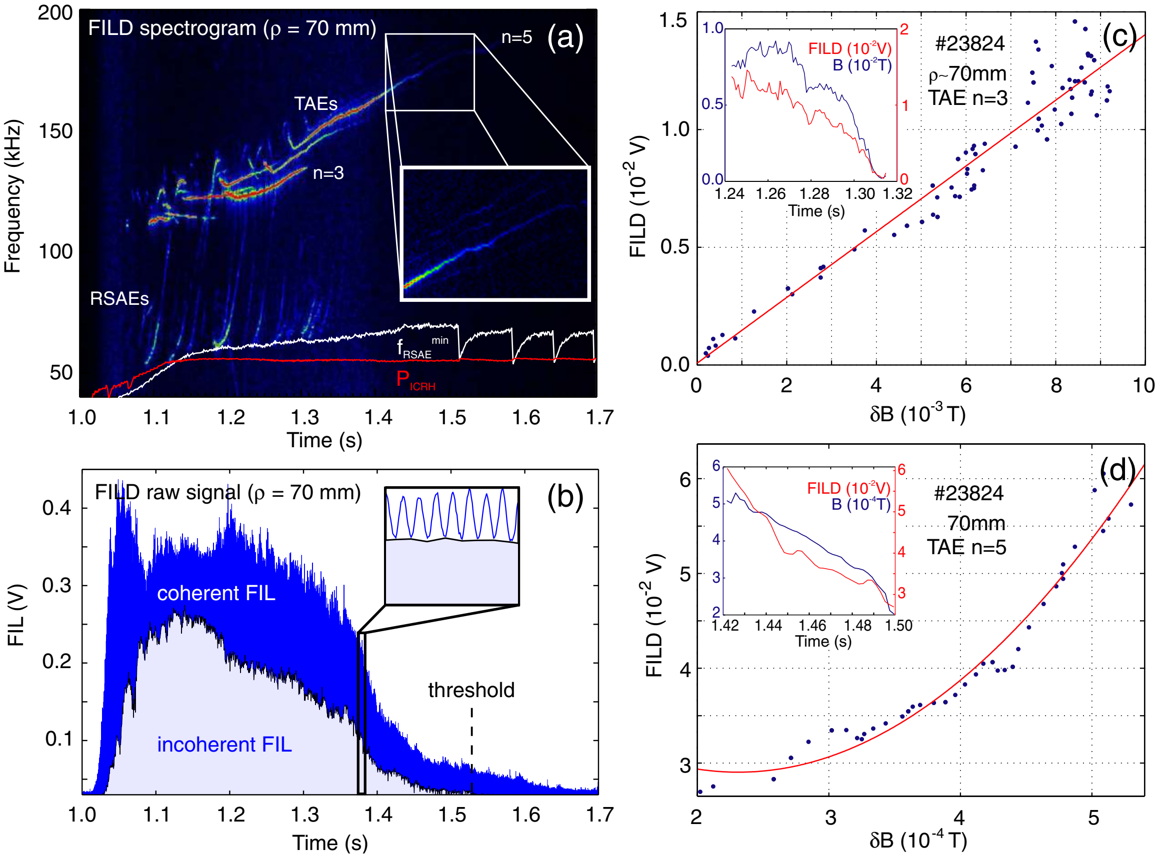

Figure 6. AUG discharge #23824. (*a*) Power spectrogram of the fast-ion loss signal with gyroradius ≈70 mm. The lowest RSAE frequency, $f_{\mathrm{RSAE}}^{\mathrm{min}}$, is superimposed in white while the total ICRH power (P_{ICRH}) is superimposed in red. The inset shows the single TAE responsible for the onset of the incoherent losses. (*b*) Fast-ion loss signal. The coherent and incoherent components of the losses are highlighted. The vertical dashed line depicts the threshold for the incoherent losses. (*c*) Linear dependence of the coherent losses at the TAE $n = 3$ frequency on the MHD fluctuation amplitude. (*d*) Quadratic dependence of the incoherent losses on the TAE $n = 5$ fluctuation amplitude.

A clear quadratic dependence has been obtained, strongly suggesting a diffusive mechanism involving several resonances in phase space. This is supported by the fact that the losses cover a larger domain in velocity space when the incoherent signal is not zero. It should also be underlined that, as shown in figure 6(*b*), the incoherent component is even larger in the presence of several modes, which is also expected to induce a stochastic fast-ion transport. The experimental results presented here are in agreement with previous works carried out at other large fusion devices with similar diagnostics and MHD fluctuations of diverse nature. Indeed, the linear and non-linear fast-ion transport in the presence of various MHD fluctuations have been observed in tokamaks [50–52] as well as stellerators [16, 53, 54] highlighting the importance of a detailed understanding of the underlying physics towards the realization of commercial fusion.

Simulations with the guiding centre drift orbit code HAGIS [55] have been performed to better understand the loss mechanisms. A wave–particle exchange of canonical momentum, P_ϕ, and energy, E, takes place if the resonant condition $\Omega_{\mathrm{n,p}} = n\omega_\phi - p\omega_\theta - \omega \approx 0$ is fulfilled. Here, ω_ϕ is the fast-ion precession frequency, ω_θ the fast-ion poloidal frequency, ω the mode frequency and $\Omega_{\mathrm{n,p}}$ the resonance width. The fast-ion orbital frequencies, ω_ϕ and ω_θ, are easily calculated using the ion constants of motion; energy, magnetic moment and toroidal canonical momentum, (E, μ, P_ϕ) and taking advantage of the characteristics of the ICRH fast-ion distribution function. For on-axis RF heated discharges, fast-ions are mostly on banana orbits with their turning points (banana tips) within the ICRH resonance layer (a vertical line passing through the magnetic axis). A simplified RF particle distribution function for the on-axis ICRF minority heating can be simulated by taking pitch angle $\Lambda = (\mu B_0/E) = 1$. In this especial case, the use of z and P_ϕ as the phase-space variable is equivalent at the turning points ($v_\parallel = 0$), where $P_\phi = Rm_i v_\parallel - Ze\Psi_{\mathrm{p}}(z) = -Ze\Psi_{\mathrm{p}}(z)$, with R, the magnetic axis radius, m_i, the fast-ion mass, Z, the atomic number, e, the electron charge and Ψ_{p} the poloidal flux. By plotting, $\log(1/\Omega_{\mathrm{n,p}})$ in the energy range of the fast-ions measured by FILD, we can identify the regions of phase space where a resonant interaction could occur [56, 57]. Figures 7(*a*)–(*f*) show the possible wave–particle resonances between the trapped fast-ions generated by the on-axis ICRF heating, i.e. with the banana tips along a vertical line at the magnetic axis, and the single AE fluctuations present in the plasma at $t = 1.16$ s. One can easily see that the low-energy region of the fast-ion phase space is virtually covered by wave–particle resonances even in the presence of single fluctuations while the high energy region ($E \geqslant 0.5$–0.6 MeV) presents some resonances only with certain AE fluctuation frequencies at ≈100 kHz (panels (*c*) and (*d*)). The last panel (*g*) shows all possible wave–particle resonances with the AEs causing coherent fast-ion

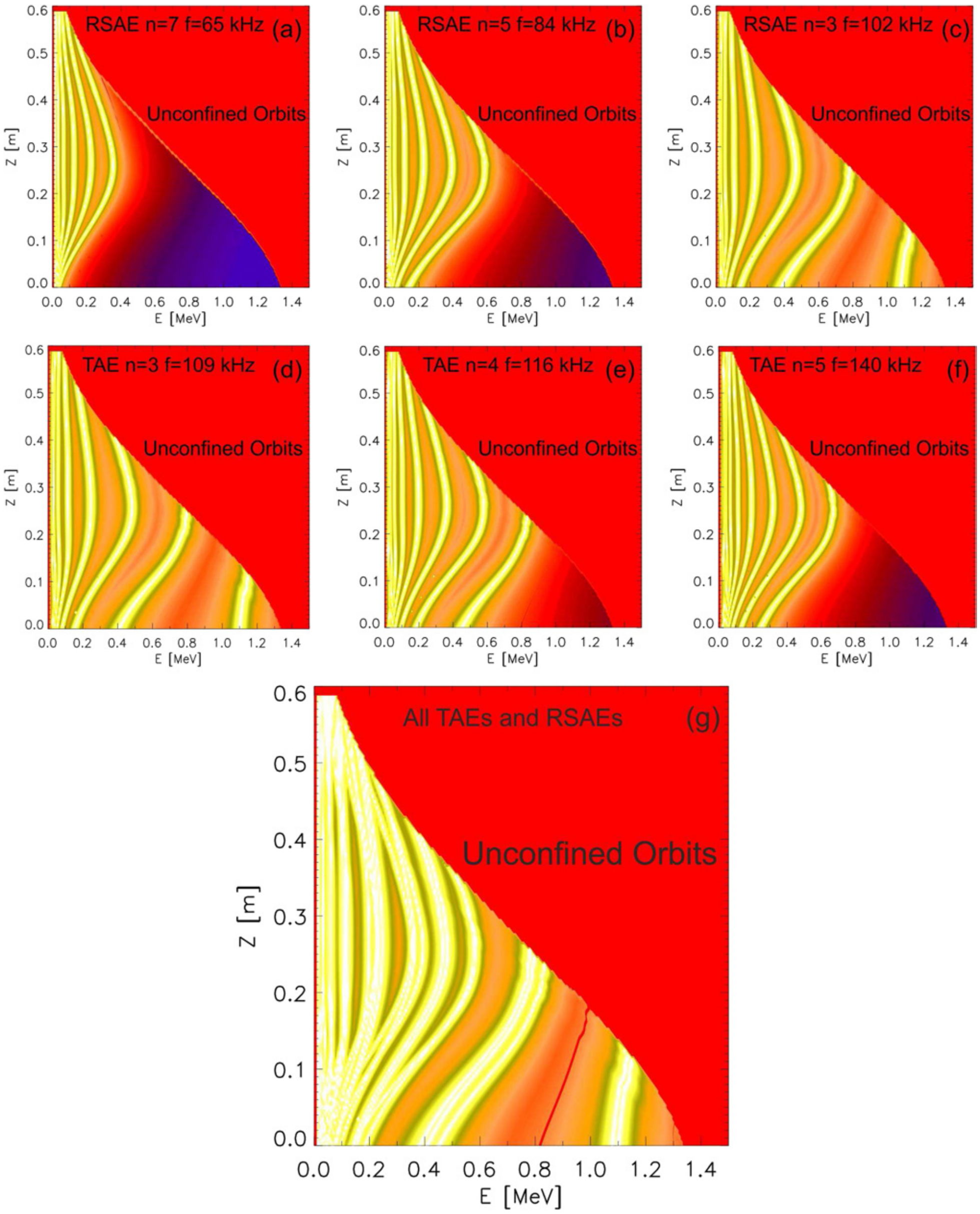

Figure 7. AUG discharge #23824. Possible wave–particle resonances between the ICRH generated fast-ions and the AEs causing coherent fast-ion losses at $t = 1.16$ s. The colour table represents the resonance width given by $\log(1/\Omega_{\mathrm{n,p}})$ with $\Omega_{\mathrm{n,p}} = n\omega_\phi - p\omega_\theta - \omega$. Panels (*a*)–(*f*) show the possible wave–particle resonances due to single AEs while panel (*g*) present all possible AE-particle resonances in plasma at $t = 1.16$ s.

losses at $t = 1.16$ s. The resulting high density of resonances suggests a stochastic transport though detailed non-linear HAGIS simulations with different q-profiles are underway to estimate the convective and stochastic contribution to the total ion loss.

3. Alfvén eigenmodes and associated fast-ion transport in NBI heated discharges

NBI is a standard heating system in present magnetically confined fusion devices. Indeed, in many machines, it is the primary source of auxiliary heating, particles and torque. A thorough understanding of the beam behaviour (deposition profile, steady state fast-particle distribution function, injection energy, etc) is crucial for plasma operation and it is therefore typically available. This information makes the NBI system a reliable tool for quantitative analysis of MHD stability and fast-ion transport to for instance benchmark numerical tools.

3.1. Alfvén eigenmodes

In AUG, AEs are driven unstable by sub-Alfvénic NBI ions during the current ramp-up phase with relative high off-axis minimum of the safety factor. The plasma density is kept at a relatively low value of $\approx(2\text{–}3) \times 10^{19}\,\mathrm{m}^{-3}$, so the fast-ion pressure is a significant fraction of the total plasma pressure. The discharge is initially in limiter configuration and switches to divertor configuration at $t \approx 0.5$ s. Throughout the period of interest, the NBI system is injecting deuterium neutrals with a main energy of 60 keV thus producing sub-Alfvénic deuterium

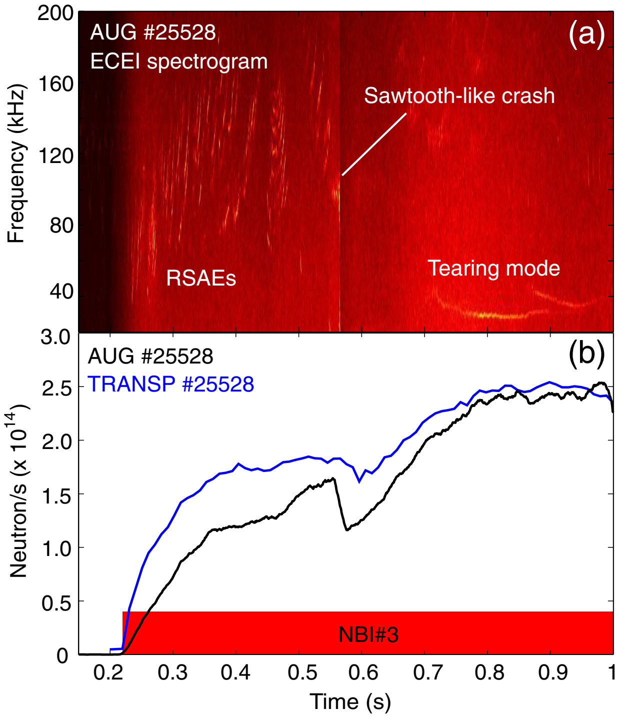

Figure 8. AUG discharge #25528. (*a*) Power spectrogram of the NBI driven AE electron temperature fluctuation measured by the ECE-imaging system (averaged over all 104 available ECEI channels). (*b*) Temporal evolution of the measured (black) and predicted by TRANSP (blue) neutron rates.

ions. In the first 550 ms a large number of RSAEs in the frequency range between ≈30 and ≈200 kHz are observed by the ECEI system, see figure 8(*a*). The RSAE activity is abruptly stopped by a sawtooth-like crash which causes an electron temperature drop of ≈30% with little change in the density profile. It is important to note that no fluctuation monitor has detected any TAE fluctuation in this discharge. As a global monitor of the AEs present in the plasma, figure 9 presents the density and temperature fluctuations measured by the reflectometer (*b*) and ECEI (*c*) systems. The reflectometer probing frequency was set at 48 GHz which corresponds to a density cutoff $n_e = 2.86 \times 10^{19}\,\mathrm{m}^{-3}$. A good estimate for the minimum frequency of the RSAEs, $f_{\mathrm{RSAE}}^{\mathrm{min}}$ (white time trace in figure 8(*c*)) is obtained with the geodesic acoustic frequency, given in section 2.1, corrected by the plasma rotation, ≈6 kHz. Toroidal rotation values are obtained directly from charge exchange recombination (CER) measurements of impurity ion rotation. Based on a simple model for the RSAE frequency [15], the temporal evolution of $q_{\min}$ can be estimated. The RSAE frequency sweeping behaviour can accurately be described by a simple model of the mode transitioning from a cylindrical mode with one dominant poloidal harmonic and localized in the weak-shear region of tokamak plasmas near a $q_{\min}$ to a TAE mode formed by the coupling of two adjacent poloidal harmonics. The sweeping rate of the frequency is tied to the temporal evolution of the $q_{\min}$ present in the plasma. In the zero plasma pressure limit, as $q_{\min}$ decreases from $q_{\min} = m/n$ to $q_{\min} = (m-1/2)/n$, the mode frequency changes from zero to the TAE frequency at $q_{\min}$ given by $f_{\mathrm{TAE}} = V_A/4 \cdot q_{\mathrm{TAE}} \cdot R$, where $q_{\mathrm{TAE}} = (m-1/2)/n$, V_A is the Alfvén speed and R is the major radius. Thus, for a decreasing $q_{\min}$, the frequency sweeps according to

$$2 \cdot \pi \cdot f_{\mathrm{RSAE}} = k_{\|} \cdot V_A = \frac{(m - n \cdot q_{\min}) \cdot V_A}{q_{\min} \cdot R}. \qquad (2)$$

Modelling results for the expected RSAE frequencies, based on this equation, are shown in figure 9(*d*) corrected with an offset given by the plasma rotation and the geodesic acoustic frequency presented in equation (1). The exact timing of half-integer and integer of $q_{\min}$ temporal crossing is obtained by matching model results with the reflectometry and ECEI spectrograms, figures 9(*b*) and (*c*).

The final $q_{\min}(t)$ used for figure 9(*d*) is a polynomial fit to the half-integer and integer crossings determined from reflectometry/ECEI data that are shown in blue in figure 9(*e*). Each eigenfrequency for a given (m, n) combination is plotted in figure 9(*d*) versus time where $m/n > q_{\min} > (m-1/2)/n$ and $f < \alpha \cdot f_{\mathrm{TAE}}$, where $\alpha = 1$ is approximated as a constant and was chosen as to be consistent with the data. The modelling results are for $m = n + l (l = 0–12)$ with the different colours corresponding to different n-values ($n = 2–12$). The vertical yellow dashed lines indicate the half-integer and integer crossing times. This simple model based on a non-computational intensive identification of the RSAEs has been successfully applied to the reconstruction of $q_{\min}(t)$ in several machines [15, 58] and is presented here for the AUG tokamak, confirming the relevance of this model for MHD spectroscopy [12].

The ratio of the Alfvén speed to the beam injection velocity, V_A/V_b, has been calculated for the RSAE radial position as well as for the typical TAE radial position in AUG, figure 9(*e*). The higher densities in the plasma core reduce the Alfvén speed, increasing the number of fast-particles that may become resonant with the AE waves as $V_A/V_b < 3$ during the whole time window. On the other hand, the lower densities typically observed at r_{TAE} (compared with the core density) increase the ratio $V_A/V_b > 4$ excluding the main wave–particle resonances. This may explain the absence of TAEs in the present discharge. Indeed, when the fast-particle source (NBI beam) is replaced with a different beam with similar injection geometry but higher injection energy (93 keV) several TAEs are driven unstable. RSAEs and TAEs are then clearly visible in the magnetic power spectrogram (figure 12(*b*)) while the ECEI power spectrogram, figure 12(*c*), shows RSAEs in the frequency range between ≈60 kHz and ≈200 kHz.

3.2. *Fast-ion transport*

The global impact that this AE activity has on the fast-ion population and fusion performance is shown in figure 8(*b*) through the measured and classically predicted neutron rates. In the presence of NBI driven RSAEs a clear deficit of neutrons is observed when comparing the measured neutron rates with that predicted by TRANSP. In the baseline discharge, #25528, the neutron rate steadily increases throughout the current ramp as soon as the NBI is switched on. TRANSP predicts (blue time trace in figure 8(*b*)) a neutron rate of up to ≈40% higher then the measured one (black time trace in figure 8(*b*)). As the RSAEs disappear the measured neutron rate starts recovering,

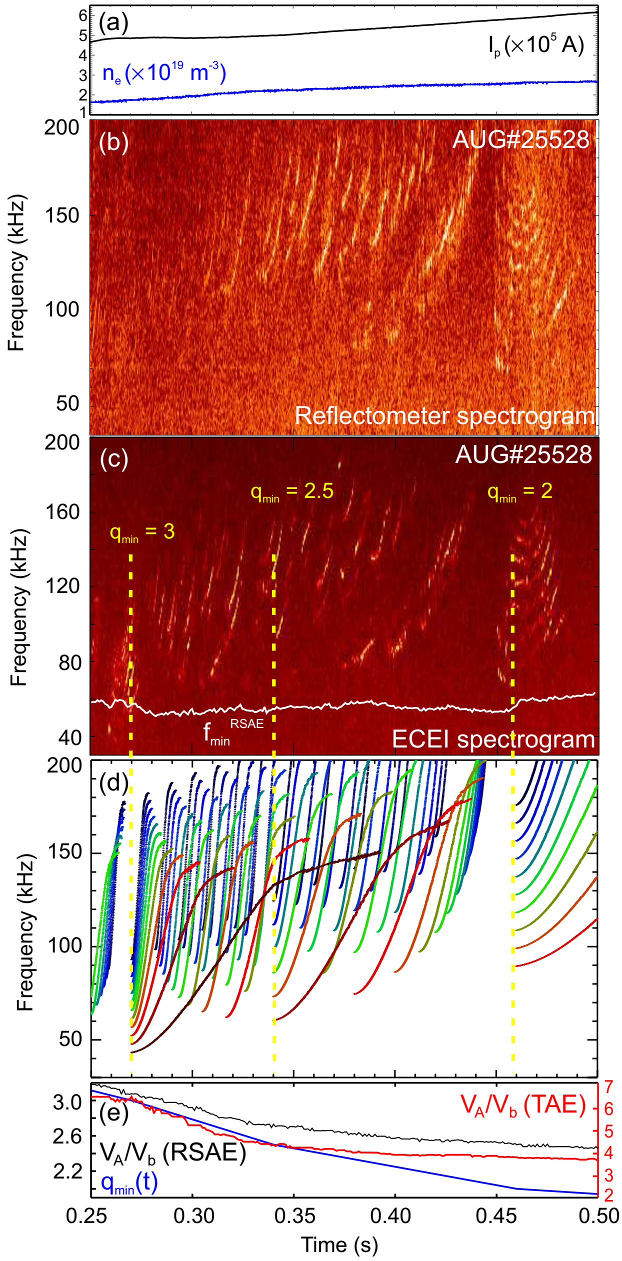

Figure 9. AUG discharge #25528. (*a*) Plasma current and density. (*b*) Power spectrogram of the AE fluctuations measured by the reflectometry system. (*c*) Averaged power spectrogram of the AE electron temperature fluctuation measured by the ECE-imaging system. (*d*) Model predictions for RSAE frequencies based on equation (2). Different colours indicate different n. For the simulation, $n = 2$–12 and $m = n + l$ where $l = 0$–12. Vertical yellow dashed lines indicate rational $q_{\min}$ crossings. (*e*) In blue, $q_{\min}(t)$ inferred from ECEI/reflectometry data and the modelling shown in panel (*d*), in black and red are plotted the temporal evolution of the ration of the Alfvén speed to the beam injection velocity , V_A/V_b, for the RSAE and TAE approx position.

matching the classical rate predicted by TRANSP when no MHD activity is present in the plasma at $t \approx 1.0$ s.

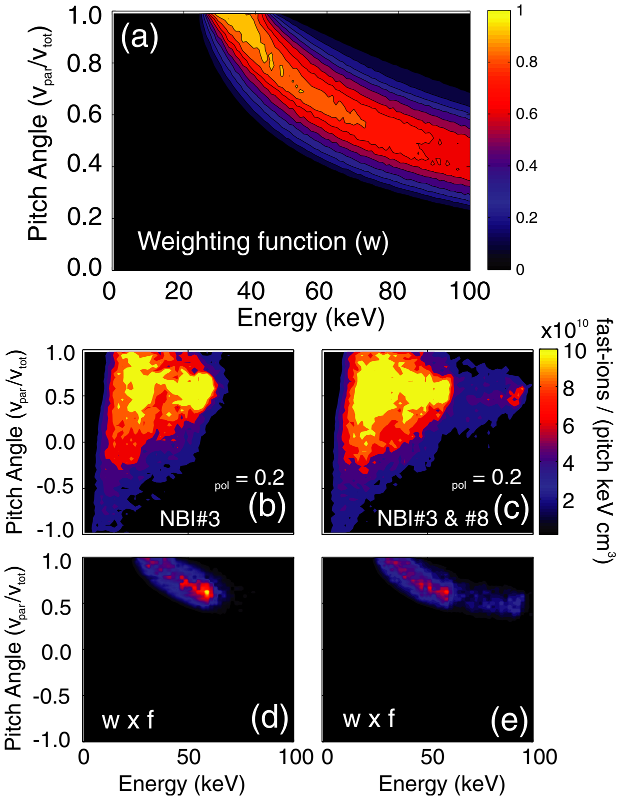

Figure 10. FIDA weighting function. (*a*) Velocity space weighting function calculated for a central line of sight of the toroidal FIDA diagnostic and for wavelengths between 659.5 and 660.5 nm. (*b*) and (*c*) show the different velocity spaces of fast ions injected by NBI3 (*b*) and NBI3 and 8 (*c*). (*d*) and (*e*) show the product between the fast-ion velocity space and diagnostic weighting function (*a*).

In NBI heated discharges the temporal evolution of the fast-ion radial profile is monitored by the recently developed in AUG FIDA spectroscopy technique [24]. The FIDA technique is a CXRS method that makes use of the Doppler shifted Balmer alpha radiation emitted by neutralized fast ions. The radiation is mainly located along the neutral beam footprint as the neutralization of fast ions happens through charge exchange reactions with injected and halo neutrals. The quick photon emission, i.e. $n = 3$ to $n = 2$ transition, enables a high spatial resolution. Using multiple lines of sight that cross the probing NBI beam at different radial positions, valuable information on the fast-ion profile can be obtained. The spectral shape and intensity of the FIDA spectra contain important details on the local fast-ion velocities and densities allowing the study of the dynamics of the fast-ion distribution. However, a direct interpretation of the FIDA measurement is rather challenging because of its convoluted nature. Two different methods can be applied when analyzing FIDA measurements; first, a forward model can be used to quantitatively interpret FIDA measurements. By simulating the neutralization and photon emission of fast ions that correspond to a given distribution function it is possible to calculate synthetic FIDA spectra. These can then be compared with the measurement. Second, after accounting for changes in the density profiles of injected and halo neutrals, changes in the FIDA spectra can be interpreted as variations in the fast-ion distribution function. Hence, the temporal evolution of the fast-ion distribution function can be studied e.g. in the presence of MHD activity.

The FIDA diagnostic at AUG uses 25 toroidally viewing lines of sight that intersect the NBI #3 from the plasma edge to the centre. The relatively narrow and well defined

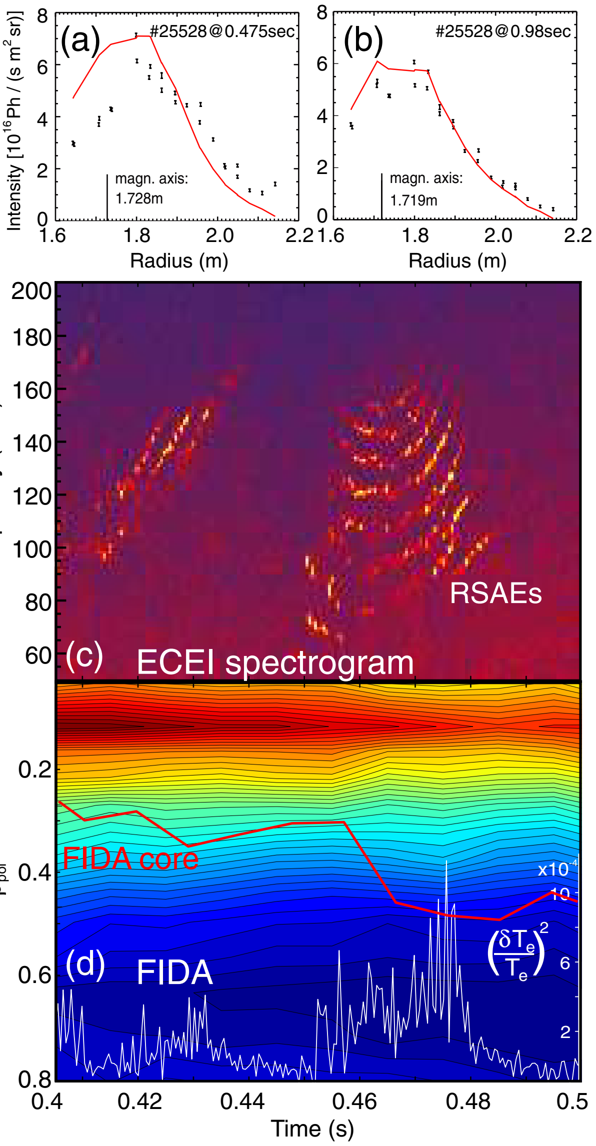

Figure 11. AUG discharge #25528. FIDA profiles at (*a*) $t = 0.475$ s and (*b*) $t = 0.98$ s. In red the FIDA profiles calculated with the FIDASIM code using measured kinetic profiles and classical fast-ion profiles predicted by TRANSP. (*c*) ECEI power spectrogram and (*d*) temporal evolution of the FIDA density profile and of the global RSAE amplitude (white curve).

area in the fast-ion velocity space covered by the AUG diagnostic viewing geometry overlaps well with the fast-ion distribution functions that are typically present in NBI heated AUG plasmas. The diagnostic observes, with a temporal resolution of 10 ms, mainly co-going fast-ions with energies above 25 keV. Figures 10(*b*) and (*c*) show the local velocity distribution of fast-ions injected by NBI #3 and #8 at $\rho_{\mathrm{pol}} \approx 0.2$. The product of these fast-ion distributions with the FIDA diagnostic weighting function is given in figures 10(*d*) and (*e*). The overall well-defined fast-ion phase space covered by the AUG FIDA diagnostic and clean FIDA spectra (without additional impurities) allow the detection of small changes in fast-ion phase space.

Radial FIDA intensity profiles are determined by integrating the FIDA radiation, observed with the 25 lines of sights, over a certain wavelength range (here 659.5–660.5 nm). In the presence of NBI driven AEs the fast-ion density profile measured by the FIDA diagnostic (black crosses in figure 11(*a*)) presents a clear depletion in the central fast-ion population, modifying strongly the fast-ion spatial gradients, when many RSAEs are unstable at the same time, $t \approx 0.475$ s, while at $t \approx 1.0$ s (figure 11(*b*)) both, measured (black crosses) and simulated profiles (red) are in excellent agreement. The classical profiles shown in red in figures 11(*a*) and (*b*) have been simulated using the FIDASIM code [59] taking the measured kinetic profiles and the classical fast-ion distribution functions predicted by TRANSP. The given error bars of the FIDA measurement are determined using the Gaussian error propagation and indicate for the photon statistics and the diagnostic readout noise. Sensitivity analysis has been performed to exclude any possible diagnostic artifacts due to finite accuracy in relevant plasma parameter measurements.

The temporal evolution of the FIDA profile during the RSAE activity, mapped on poloidal flux coordinates, is given in arbitrary units in figure 11(*d*). To account for possible changes in the FIDA radiance due to changes in the halo population and in the beam attenuation which would influence the probability for a fast-ion to undergo charge exchange reactions, approximate fast-ion density profiles were calculated. Thereby, density profiles of injected and halo neutrals were calculated for every acquired time frame. Figure 11(*d*) shows an extra drop in the central fast-ion density, as q_{min} passes through an integer (as the simultaneous occurrence of many RSAEs indicates), correlated with the maximum of a global RSAE fluctuation amplitude (white curve in figure 11(*d*)). The temporal evolution of the global RSAE fluctuation amplitude has been calculated by summing over all RSAE temperature fluctuations detected by the ECEI system. The red time trace in figure 11(*d*) indicates the temporal evolution of the central fast-ion population (mean of central FIDA channels). It is important to note that no fast-ion losses have been observed so far in AUG discharges with the solely detectable presence of NBI driven RSAEs. In fact, when many RSAEs and TAEs are unstable at the same time, the coherent fast-ion losses are dominated by the radially extended TAEs while only strong RSAEs cause some coherent fast-ion losses as figures 12(*b*)–(*d*) show. TAEs have been driven unstable replacing the 60 keV beam with a 93 keV NBI source with a similar injection geometry. Figure 12(*a*) shows the plasma density, n_{e}, plasma current, I_{p}, and ratio of the Alfvén speed to the beam injection velocity, $V_{\mathrm{A}}/V_{\mathrm{b}}$. Although the 93 keV beams in AUG are still sub-Alfvénic, as figure 12(*a*) shows, the ratio $V_{\mathrm{A}}/V_{\mathrm{b}}$ is well below 3 and so increasing the number of particles that interact resonantly with the AE waves through the resonance $V_{\mathrm{A}} = 3 \cdot V_{\mathrm{b}}$ [2]. This may help to explain the fact that with 60 keV beams no TAEs are observed. Figure 12(*b*) presents the magnetic fluctuations measured at the plasma edge by the magnetic pick up coils. In white the calculated f_{TAE} using off-axis plasma density is superimposed. Some RSAEs are also clearly visible in the magnetic power spectrogram together with other broadband modes that are not causing any coherent fast-ion losses. All electron temperature fluctuations measured in the plasma core by the ECEI system (clearly dominated by the

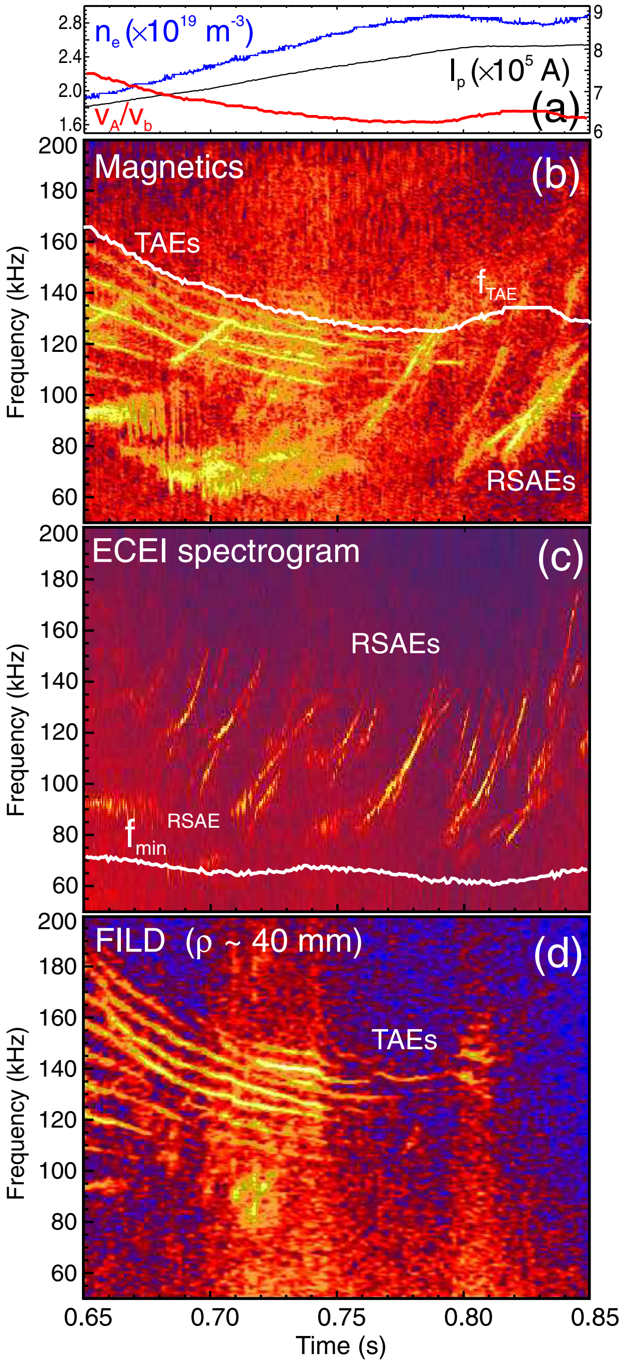

Figure 12. AUG discharge #25491. (*a*) Plasma density, n_e, and current, $I-p$, and ratio of Alfvén speed to beam injection velocity, V_A/V_b. (*b*) Power spectrogram of a magnetic pick-up coil, (*c*) Power spectrogram of the electron temperature fluctuation measured by the ECEI system and (*d*) Power spectrogram of the fast-ion losses measured by FILD.

RSAE fluctuations) are presented in figure 12(*c*) through a power spectrogram of all the available ECEI channels (104). Note that TAEs are not visible in the ECEI spectrogram because the overlapping between the ECEI observation window and the TAE radial structure is minimal. The ECEI system is looking at the plasma core where the RSAE amplitudes are maximal and TAEs rather weak. The minimum RSAE frequency has been calculated using the geodesic acoustic frequency given in equation (1) corrected with the toroidal plasma rotation, ≈9 kHz, and is superimposed in white in the ECEI spectrogram. The coherent fast-ion losses measured by the FILD system in the presence of the AE activity is shown in figure 12(*d*). The losses are clearly dominated by the TAEs while some losses correlated with the RSAE frequencies are also barely visible.

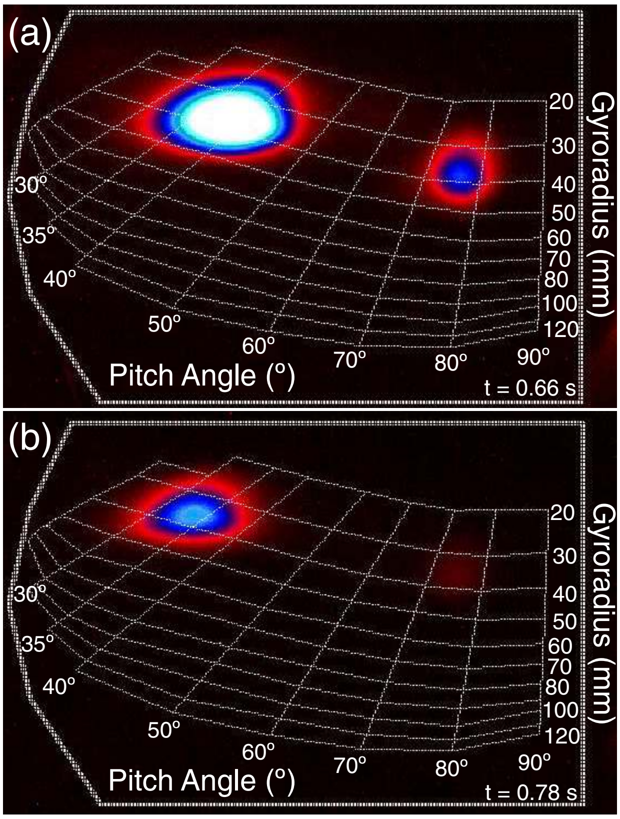

Figure 13. AUG discharge #25491. Velocity space of the escaping fast-ions measured by the FILD system at two different time points.

In order to identify the topology of the escaping fast-ion orbits, the velocity space of the measured lost ions is presented in figure 13. The escaping ions detected by the FILD system have energies close to the injection energy, 93 keV, which corresponds to a gyroradius of ≈38 mm at the probe and two well-defined pitch-angles. Both panels in figures 13(*a*) and (*b*) show the velocity space of the measured losses at two different time points with strong, $t = 0.66$ s and weak, $t = 0.78$ s, AE activity respectively.

The orbits of the expelled ions have been simulated using the full orbit code GOURDON. Ions have been started at the FILD collimator position with the right gyro-phase and the measured energy and pitch angles and followed backwards in time until they close one poloidal transit. Figure 14(*a*) shows the trajectory of the escaping deuterium ions with the injection energy and pitch angle of ≈35°–40° while figure 14(*b*) shows the same exercise but for a deuterium ion with the injection energy and a pitch angle of ≈75°–80°. It is important to note that both trapped as well as passing ions are strongly affected by AEs.

Detailed simulations with realistic first wall geometry, eigenmode structures and fast-ion distributions are necessary

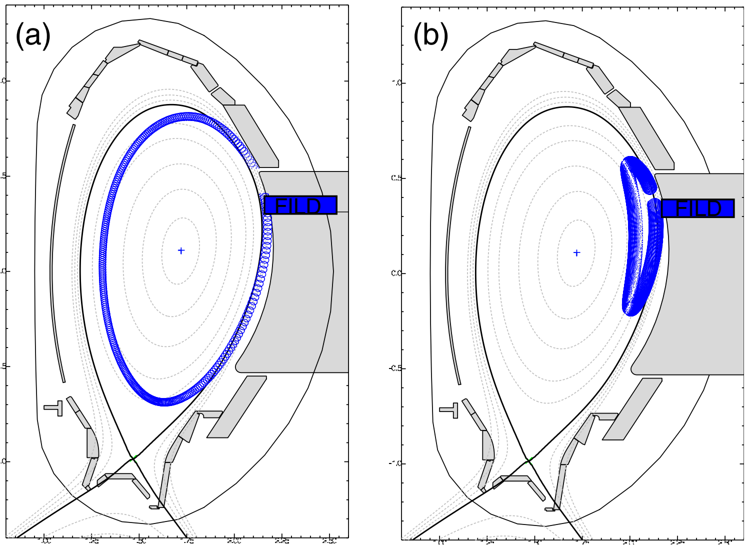

Figure 14. AUG discharge #25491. Simulated trajectories of the escaping fast-ions measured by FILD. The full orbits have been calculated using the GOURDON code.

to decouple first-order geometric effects from non-linear wave–particle interaction effects.

4. Conclusions

The fast-ion confinement in the presence of AEs has been studied in the AUG tokamak with anisotropic distribution functions provided separately by NBI and RF heating systems. The confinement of both trapped and passing ions has been observed to be strongly affected by AEs. Detailed measurements of the AE spatial structures as well as of the fast-ion redistribution and loss have allowed a better understanding of the underlying transport mechanisms. Convective and diffusive fast-ion losses induced by AEs have been measured at the plasma edge by means of a scintillator based detector. Time-resolved energy and pitch-angle measurements of the fast-ion losses correlated in frequency and phase with RSAEs and TAEs have allowed to identify both loss mechanisms. While single RSAEs and TAEs eject resonant fast-ions in a convective process directly proportional to the fluctuation amplitude, δB. The overlapping of multiple RSAE and TAE spatial structures and resonances lead to a large diffusive loss. For single TAEs, diffusive losses of fast-ions, scaling as $(\delta B)^2$, are observed for local radial displacements above a certain threshold. In NBI heated discharges, the temporal evolution of the fast-ion profile has been monitored using the FIDA technique. A large drop in the central fast-ion density due to many RSAEs as $q_{\min}$ passes through an integer has been observed. In general, radially extended TAEs are more efficient ejecting ions from the plasma than RSAEs while the latter may act as a fast-ion seed, redistributing the ions from the plasma core to the TAE area of influence, modifying considerably the fast-ion spatial gradients. Detailed simulations during the linear and non-linear phases of the AE induced fast-ion redistribution and loss will be carried out using realistic AE fluctuation amplitudes and fast-ion distribution functions with the ultimate goal of predicting the impact that a radial chain of AEs may have on ITER.

References

[1] Herrmann A. and Gruber O. 2003 *Fusion Sci. Technol.* **44** 569
[2] Heidbrink W.W. 2008 *Phys. Plasmas* **15** 055501
[3] Gorelenkov N.N. 2003 *Nucl. Fusion* **43** 594
[4] Gorelenkov N.N., Berk H. and Budny R. 2005 *Nucl. Fusion* **45** 226
[5] Heidbrink W.W. and Sadler G.J. 1994 *Nucl. Fusion* **34** 535
[6] Fasoli A. *et al* 2007 *Nucl. Fusion* **47** S264
[7] Duong H. *et al* 1993 *Nucl. Fusion* **33** 749
[8] Wong K.L. *et al* 1991 *Phys. Rev. Lett.* **66** 1874
[9] Heidbrink W.W. 1991 *Nucl. Fusion* **31** 1635
[10] Kimura H. *et al* 1998 *Nucl. Fusion* **38** 1303
[11] Berk H.L., Borba D.N., Breizman B.N., Pinches S.D. and Sharapov S.E. 2001 *Phys. Rev. Lett.* **87** 185002
[12] Sharapov S.E. *et al* 2001 *Phys. Lett.* A **289** 127
[13] Shinohara K. *et al* 2004 *Plasma Phys. Control. Fusion* **46** S31
[14] Snipes J.A. *et al* 2005 *Phys. Plasmas* **12** 056102
[15] Van-zeeland M.A. *et al* 2006 *Nucl. Fusion* **46** S880
[16] Toi K. *et al* 2011 *Plasma Phys. Control. Fusion* **53** 024008
[17] Classen I. *et al* 2010 *Rev. Sci. Instrum.* **81** 10D929
[18] Hicks N.K. *et al* 2010 *Fusion Sci. Technol.* **57** 1
[19] Igochine V., Gude A. and Maraschek M. 2010 IPP Report No **1/338**
[20] Silva A. *et al* 1999 *Rev. Sci. Instrum.* **70** 1072
[21] Heidbrink W.W., Kim J. and Groebner R.J. 1988 *Nucl. Fusion* **28** 1897
[22] Heidbrink W.W., Burrell K.H., Luo Y., Pablant N.A. and Ruskov E. 2004 *Plasma Phys. Control. Fusion* **46** 1855
[23] Garcia-munoz M., Fahrbach H.-U. and Zohm H. 2009 *Rev. Sci. Instrum.* **80** 053503
[24] Geiger B. *et al* 2011 *Plasma Phys. Control. Fusion* **53** 065010
[25] Delabie E., Jaspers R.J.E., Von Hellermann M.G., Nielsen S.K. and Marchuk O. 2008 *Rev. Sci. Instrum.* **79** 10E522
[26] Heidbrink W.W., Bell R.E., Luo Y. and Solomon W. 2006 *Rev. Sci. Instrum.* **77** 10F120
[27] Osakabe M. *et al* 2008 *Rev. Sci. Instrum.* **79** 10E519
[28] Zweben S.J. 1990 *Nucl. Fusion* **30** 1551
[29] Darrow D.S. *et al* 1995 *Rev. Sci. Instrum.* **66** 476
[30] Isobe M. 1999 *Rev. Sci. Instrum.* **70** 827
[31] Werner A., Weller A. and Darrow D.S. 2001 *Rev. Sci. Instrum.* **72** 780
[32] Darrow D. 2001 *Rev. Sci. Instrum.* **72** 2936
[33] Nishiura M., Isobe M., Saida T., Sasao M. and Darrow D.S. 2004 *Rev. Sci. Instrum.* **75** 3646

[34] Baeumel S. *et al* 2004 *Rev. Sci. Instrum.* **75** 3563
[35] Darrow D., Fredrickson E., Gorelenkov N., Roquemore A. and Shinohara K. 2008 *Nucl. Fusion* **48** 084004
[36] Jimenez-Rey D. *et al* 2008 *Rev. Sci. Instrum.* **79** 093511
[37] Fisher R.K. *et al* 2010 *Rev. Sci. Instrum.* **81** 10D307
[38] Pace D.C. *et al* 2010 *Rev. Sci. Instrum.* **81** 10D305
[39] Garcia-munoz M. *et al* 2010 *Phys. Rev. Lett.* **104** 185002
[40] Garcia-munoz M. *et al* 2010 *Nucl. Fusion* **50** 084004
[41] Nazikian R. *et al* 2008 *Phys. Plasmas* **15** 056107
[42] Garcia-munoz M. *et al* 2008 *Phys. Rev. Lett.* **100** 055005
[43] Cheng C. and Chance M. 1987 *J. Comput. Phys.* **71** 1124
[44] Breizman B.N., Pekker M.S. and Sharapov S. 2005 *Phys. Plasmas* **12** 112506
[45] Van-zeeland M.A. *et al* 2006 *Phys. Rev. Lett.* **97** 135001
[46] Borba D. *et al* 2004 *Plasma Phys. Control. Fusion* **46** 809
[47] Sassenberg K. *et al* 2009 *Plasma Phys. Control. Fusion* **51** 065003
[48] Brambilla M. 1999 *Plasma Phys. Control. Fusion* **41** 1
[49] Brambilla M. 1994 *Nucl. Fusion* **34** 1121
[50] Heidbrink W.W., Hay R. and Strachan J.D. 1984 *Phys. Rev. Lett.* **53** 1905
[51] Darrow D.S. *et al* 1997 *Nucl. Fusion* **37** 939
[52] Zeeland M.A.V. *et al* 2011 *Phys. Plasmas* **18** 056114
[53] Nagaoka K. *et al* 2008 *Phys. Rev. Lett.* **100** 065005
[54] Ogawa K. *et al* 2010 *Nucl. Fusion* **50** 084005
[55] Pinches S.D. 1998 *Comput. Phys. Commun.* **111** 131
[56] Berk H.L., Breizman B.N., Fitzpatrick J. and Wong H.V. 1995 *Nucl. Fusion* **35** 1661
[57] Pinches S.D., Kiptily V.G., Sharapov S.E. and Darrow D.S. 2006 *Nucl. Fusion* **46** S904
[58] Sharapov S. *et al* 2006 *Nucl. Fusion* **46** S868
[59] Heidbrink W.W., Liu D., Luo Y., Ruskov E. and Geiger B. 2011 *Commun. Comput. Phys.* **10** 716